Available online at www.sciencedirect.com
SCIENCE DIRECT®
Journal of Magnetic Resonance 168 (2004) 175–185
JMR Journal of Magnetic Resonance
www.elsevier.com/locate/jmr

NMR acceleration mapping in percolation model objects

Bogdan Buhai,[a] Aidar Hakimov,[a] Ioan Ardelean,[b] and Rainer Kimmich[a,*]

[a] *Sektion Kernresonanzspektroskopie, Universität Ulm, 89069 Ulm, Germany*
[b] *Department of Physics, Technical University, 3400 Cluj-Napoca, Romania*

Received 19 December 2003; revised 18 February 2004

Abstract

An NMR microscopy technique is described that permits direct mapping of local accelerations. The method is tested with water flow through a random site percolation model object and compared with computational fluid dynamics simulations. A general formalism, the ''polygon rule,'' is reported for the design of gradient pulse sequences for phase encoding of higher order motions, or, in other words, for compensation of phase shifts by lower motional orders.

Keywords: Acceleration; NMR mapping; Percolation; Porous media

1. Introduction

In recent papers [1–5] we have reported on microscopic NMR mapping experiments and simulations of transport in fluid filled percolation model objects of porous media. The objective was to study and learn the laws governing coherent or incoherent propagation of measurands specifying transport under complex pore space constraints. Phenomena of interest so far were coherent flow characterized by velocity maps, incoherent flow, and diffusion leading to hydrodynamic dispersion, thermal conduction, and convection causing temperature distributions and hydrodynamic flow patterns, and electric currents in electrolyte solutions. A comprehensive description of such methods can be found in recent reviews [6,7].

The advantage of percolation model objects first simulated as templates on a computer and then fabricated with the aid of milling [8] or lithography [9] techniques is in the first place that pore space topologies based on well-defined generation algorithms can be realized. Another advantage is that the boundary conditions of the pore space are known and can directly be used for numerical simulations of the transport quantities. Such simulations help to plan and design experiments properly so that time and effort consuming failures are avoided. Comparisons of experimental data and their simulated counterparts permit one moreover to judge the reliability both of the numerical simulation method and of the measuring technique. The meaningfulness of such combined study is thus particularly well founded.

In the present paper we report on an NMR method for direct mapping of locally stationary accelerations of liquids flowing through porous systems. Of course, having a velocity map in principle implies the information on local accelerations as well. However, flow measurements with the standard phase encoding technique anticipates [10–12] *constant* velocities so that the existence of any acceleration leads to additional phase shifts causing experimental velocity artefacts. Even if a velocity map were available with the required accuracy, it always refers to *average* values in the voxels resolved in the experiment. Reconstructing particle trajectories based on such voxel-average velocities and from these local accelerations unavoidably entails strong errors as test experiments demonstrated. The error of such evaluations depends on the spatial variation of the velocity field and the spatial resolution of the mapping experiment. In other words, the correlation length of the velocity field must be much larger than the spatial resolution in order to obtain reliable acceleration vectors from a velocity vector field.

* Corresponding author. Fax: +49-731-5023150.
E-mail address: rainer.kimmich@physik.uni-ulm.de (R. Kimmich).

1090-7807/$ - see front matter © 2004 Elsevier Inc. All rights reserved.
doi:10.1016/j.jmr.2004.02.013

In order to avoid this difficulty it appears to be worthwhile to directly phase encode accelerations while phase shifts by velocities stationary with respect to magnitude and direction are suppressed. Such direct mapping experiments are expected to result in more reliable voxel-average accelerations. The condition is that the local acceleration is stationary in order to avoid any higher-order phase encoding errors. This, however, is not a problem, since the relatively low time resolution of NMR microscopy always stipulates stationarity on an imaging time scale of several minutes if not hours. Rapidly time variable flow patterns as they occur in turbulent flow [13–15] can be studied by NMR only in the frame of particularly favourable time resolutions. Here we focus on laminar flow where the local velocity vector is a function of position but not of time.

2. The acceleration mapping technique

The basic element of phase encoding of accelerations is a sequence of bipolar field gradients as illustrated in Fig. 1. The effect of such gradient pulses is a phase shift of the spin coherences proportional to the local acceleration whereas phase shifts by stationary velocities and for static nuclei are compensated [11,12,16].

Consider the trajectory of a nucleus as a function of time. The position component along the field gradient, which is arbitrarily assumed along the x direction of the laboratory frame, evolves according to the following Taylor series:

$$x(t) = x_0 + v_{x0}t + \frac{a_{x0}}{2}t^2 + \cdots, \tag{1}$$

where x_0, v_{x0}, and a_{x0} are the initial position, velocity, and acceleration components, respectively. Higher order terms (referring to locally time-dependent accelerations) must be neglected due to the low time resolution intrinsic to magnetic resonance imaging experiments. The experiments to be described below were furthermore performed under conditions of locally *stationary* accelerations: All higher order terms therefore vanish by definition. Stationary flow patterns and pressure gradients stipulate locally stationary velocities and accelerations. Note that we record accelerations of spins being *at certain positions* (voxels) during the measurements rather than accelerations of a certain tracer particle experiencing varying accelerations when travelling through different voxels.

The phase shift adopted in the presence of a field gradient, $G_x = G_x(t)$, in the period $0 \leqslant t \leqslant T$ is

$$\phi(T) = \int_0^T \Omega[x(t)]\,\mathrm{d}t = \gamma_n \int_0^T G_x(t)x(t)\,\mathrm{d}t, \tag{2}$$

where $\Omega(x) = \gamma_n G x$ is the angular frequency offset at the position $x = x(t)$ due to the spatially constant field gradient. Inserting Eq. (1) in Eq. (2) gives

$$\begin{aligned}\Phi(T) &= \gamma_n \left[x_0 \underbrace{\int_0^T \zeta(t)G_x(t)\,\mathrm{d}t}_{m_0} + v_{x0} \underbrace{\int_0^T \zeta(t)G_x(t)t\,\mathrm{d}t}_{m_1} \right. \\ &\quad \left. + \frac{1}{2}a_{x0} \underbrace{\int_0^T \zeta(t)G_x(t)t^2\,\mathrm{d}t}_{m_2} \right] \\ &= \Phi_0(T) + \Phi_1(T) + \Phi_2(T),\end{aligned} \tag{3}$$

where γ_n is the gyromagnetic ratio and m_n ($n = 0, 1, 2$) is the nth moment of the gradient pulse sequel during the interval T. The function $\zeta(t)$ accounts for the phase reversal by the 180° RF pulse in the middle of the spin echo pulse sequence (see Fig. 1):

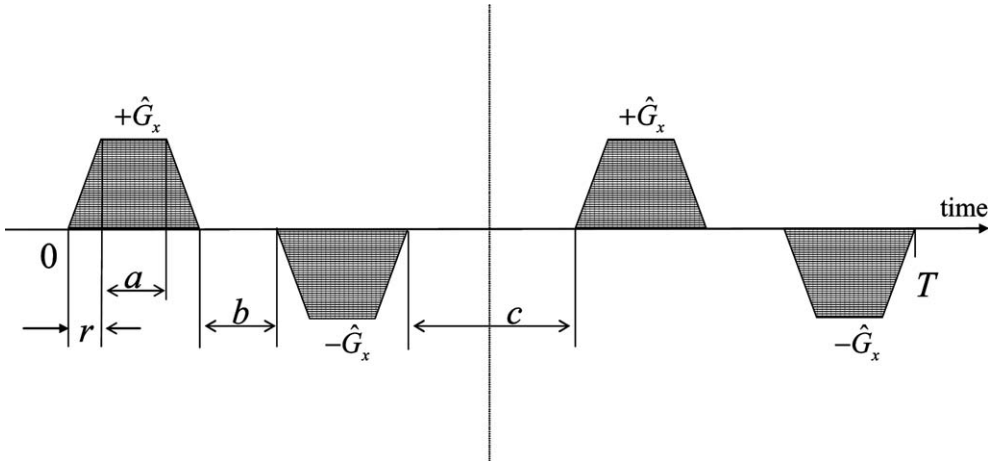

Fig. 1. Bipolar field gradient pulses symmetric to the 180° radio frequency (RF) pulse (dotted line) of a spin-echo sequence. Phase shifts of spin coherences proportional to the second moment, and, hence, to the local acceleration are generated, whereas the zeroth and first moment vanish. That is, field gradient pulses of this sort suppress any phase shifts due to position and constant velocity.

$$\zeta(t) = \begin{cases} +1 & \text{before the } 180^\circ \text{ pulse,} \\ -1 & \text{after the } 180^\circ \text{ pulse.} \end{cases} \quad (4)$$

The problem is now to make the zeroth and first moments vanish while the second moment remains finite. The simplest solution is the sequence shown in Fig. 1. The zeroth and first moments obviously vanish, i.e.,

$$\begin{aligned} \Phi_0(T) &= \gamma_n x_0 \int_0^T \zeta(t) G_x(t)\,\mathrm{d}t \\ &= \gamma_n x_0 \int_0^{4a+2b+c+8r} \zeta(t) G_x(t)\,\mathrm{d}t = 0 \end{aligned} \quad (5)$$

and

$$\begin{aligned} \Phi_1(T) &= \gamma_n v_{x0} \int_0^T \zeta(t) G_x(t) t\,\mathrm{d}t \\ &= \gamma_n v_{x0} \int_0^{4a+2b+c+8r} \zeta(t) G_x(t) t\,\mathrm{d}t = 0. \end{aligned} \quad (6)$$

The coherence phase shift due to the second moment reads

$$\begin{aligned} \Phi_2(T) &= \frac{1}{2}\gamma_n a_{x0} \int_0^T \zeta(t) G_x(t) t^2\,\mathrm{d}t \\ &= \frac{1}{2}\gamma_n a_{x0} \int_0^{4a+2b+c+8r} \zeta(t) G_x(t) t^2\,\mathrm{d}t \\ &= \frac{1}{2}\gamma_n a_{x0} \hat{G}_x \big(16r^3 + 4a^3 + 20a^2 r + 32ar^2 + 2ab^2 \\ &\quad + 6a^2 b + 2b^2 r + 12br^2 + 4a^2 c + 8cr^2 \\ &\quad + 4acb + 4cbr + 12acr + 18abr\big) \propto a_{x0}. \end{aligned} \quad (7)$$

This phase shift is proportional to the local acceleration and will be taken as the quantity to be mapped in the experiments.

The complete pulse sequence for the acceleration maps is schematically shown in Fig. 2 (leaving the gradient pulse ramps away for simplicity). In this pulse sequence, phase encoding of the acceleration components and spatial encoding for the mapping are

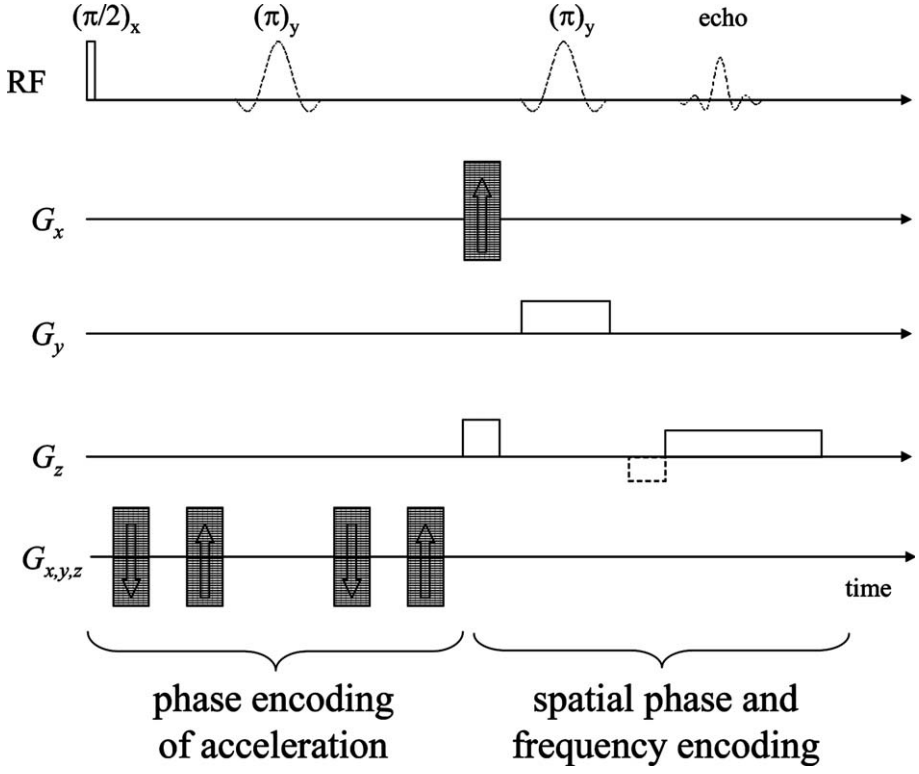

Fig. 2. Typical RF and field gradient pulse sequence used for NMR acceleration mapping experiments. A standard (secondary) Hahn spin echo imaging sequence is used in combination with two pairs of bipolar gradient pulses. The ramps of the gradient pulses are not shown for simplicity. The (second) π pulse is applied in the presence of a gradient G_y and serves the selection of the desired slice. The other two spatial dimensions are probed by gradient pulses G_z (frequency encoding) and G_x (phase encoding). The phase encoding gradient, G_x is incremented in a series of successive transients. To acquire the acceleration vector field, all three components must be probed one by one. These components are phase encoded by the first two pairs of bipolar gradient pulses which are also incremented in a series of (in our case nine) transients. For quasi two-dimensional objects as they are studied in the present investigation, the data set acquired in this way consists of two four-dimensional matrices. Fourier transforms in all four dimensions lead to conjugated data sets describing the two in-plane acceleration vector components for each voxel. The imaging part of the pulse sequence is kept particularly short in order to avoid flow phase encoding by gradient pulse pairs. In critical situations it is more favourable to place the refocusing pulse of the read gradient in the form of a negative lobe directly before the read gradient pulse in order to reduce the undesired phase encoding further (lobe drawn with broken lines).

performed in two separate free-evolution intervals of the spin coherences by using a secondary Hahn echo RF pulse sequence. In principle, all phase encoding could be done simultaneously in one free-evolution interval of an ordinary spin echo sequence, since the gradient pulses are incremented independently from each other. However, from the practical standpoint it turned out that the sequential employment of the acceleration and position phase-encoding pulses leads to more stable and reliable results.

A certain source of experimental artefacts is that the gradient pulses used in the second (imaging) half of the pulse sequence are not compensated for phase shifts by velocities. That is, the spatial phase-encoding dimension of the imaging process may be affected by such spurious phase shifts. In principle this could be avoided by the use of "velocity (and acceleration) compensated" gradient pulses [11,12]. However, the pulse would then become too complicated. We therefore preferred to keep the imaging part so short that such artefacts practically did not matter. A generalized design rule for gradient pulses compensating motion induced phase shifts of any order [17] will be presented in the Appendix.

3. Model objects and instruments

The proposed technique was tested with liquid flow through two different pore space model objects shown in Figs. 3A and B. Computational fluid dynamics simulations were moreover performed for the same pore space topologies and under the same flow conditions. The test object represented by Fig. 3A was designed on a computer using the software package Gambit 2.1. The more complex percolation cluster in Fig. 3B was produced with the aid of a random number generator. Both computer-generated pore space structures were fed to a digital circuit board plotter (LPKF, "Leiterplatten–Konturfräsen") for milling the pore space into 3 mm thick polystyrene plates [1]. The milling depth was 2 mm and the position resolution of the milling machine was 6.35 μm.

The samples were composed of stacks of 10 identical quasi two-dimensional model objects in order to improve the signal-to-noise ratio. The pore space was filled with water. It was taken care that no gas bubbles occurred. Constant flow during the experiment was ensured by the hydrostatic pressure resulting from a reservoir 1.5 m above the sample level. The reservoir was permanently refilled with the aid of a peristaltic pump. The total flow rate was in the range 0.1–0.3 ml/s. The water was doped with $CuSO_4$ in order to reduce the spin–lattice relaxation time T_1 to about 500 ms. The Reynolds number is estimated to be $Re = 0.2$, which is far below the critical value where turbulence starts to become effective.

Acceleration maps were recorded using the pulse sequence shown in Fig. 2. The imaging parameters were: repetition time $T_R = 2$ s, number of scans $N_s = 16$, echo time $T_E = 22$ ms. The tomograph consisted of a home made RF console and a 4.7 T magnet with a horizontal 40 cm room temperature bore. The resonator was of the birdcage type. The maximum gradient was 50 mT/m in each direction (x, y, and z). All measurements were performed at room temperature.

4. Computational fluid dynamics simulation method

The computational fluid dynamics simulations were performed on a PC using the software package FLUENT 5.5.14 based on the finite volume method (FVM). For rendering maps the package IDL 5.3 was employed.

In the case of the circle arc test object the mesh used was of QUAD type (see [19] for more details). The channels were subdivided into a minimum of six smaller subchannels. The resulting extension of the "finite" elements was 60 μm × 60 μm. The mesh net was finer in the interior of the channels in order to achieve a better convergence of the solution.

In the case of the random percolation model each matrix point was represented by 5 × 5 "knots" or "elements." The convergence criteria was set to a residuum of 10^{-5}. Obstacles in the pore space are defined by vanishing flow velocity at the corresponding knots. In this way periodic meshing was possible so that the same resolution, 60μm × 60μm, applies to all flow paths. In the simulation the same parameters (fluid viscosity, pressure difference exerted to the object, and object size) were assumed as in the NMR experiments.

The simulation of acceleration maps requires a consideration different from the experimental procedure. The FVM method used in the software package FLUENT 5.5 does not allow direct rendering of acceleration maps. Rather, processing of velocity maps was necessary based on the software package IDL 5.3. For these derivations an Eulerian approach was employed anticipating the two-dimensional velocity vector field corresponding to our quasi two-dimensional model objects:

$$\vec{v} = (v_x(x,y,t), v_y(x,y,t)). \tag{8}$$

The local acceleration components in the object plane are then given by

$$\begin{aligned} a_x = a_x(x,y) &= \frac{\mathrm{d}v_x}{\mathrm{d}t} = \frac{\partial v_x}{\partial t} + \frac{\partial v_x}{\partial x}\frac{\partial x}{\partial t} + \frac{\partial v_x}{\partial y}\frac{\partial y}{\partial t} \\ &= \frac{\partial v_x}{\partial t} + \frac{\partial v_x}{\partial x}v_x + \frac{\partial v_x}{\partial y}v_y, \end{aligned} \tag{9}$$

$$\begin{aligned} a_y = a_y(x,y) &= \frac{\mathrm{d}v_y}{\mathrm{d}t} = \frac{\partial v_y}{\partial t} + \frac{\partial v_y}{\partial x}\frac{\partial x}{\partial t} + \frac{\partial v_y}{\partial y}\frac{\partial y}{\partial t} \\ &= \frac{\partial v_y}{\partial t} + \frac{\partial v_y}{\partial x}v_x + \frac{\partial v_y}{\partial y}v_y. \end{aligned} \tag{10}$$

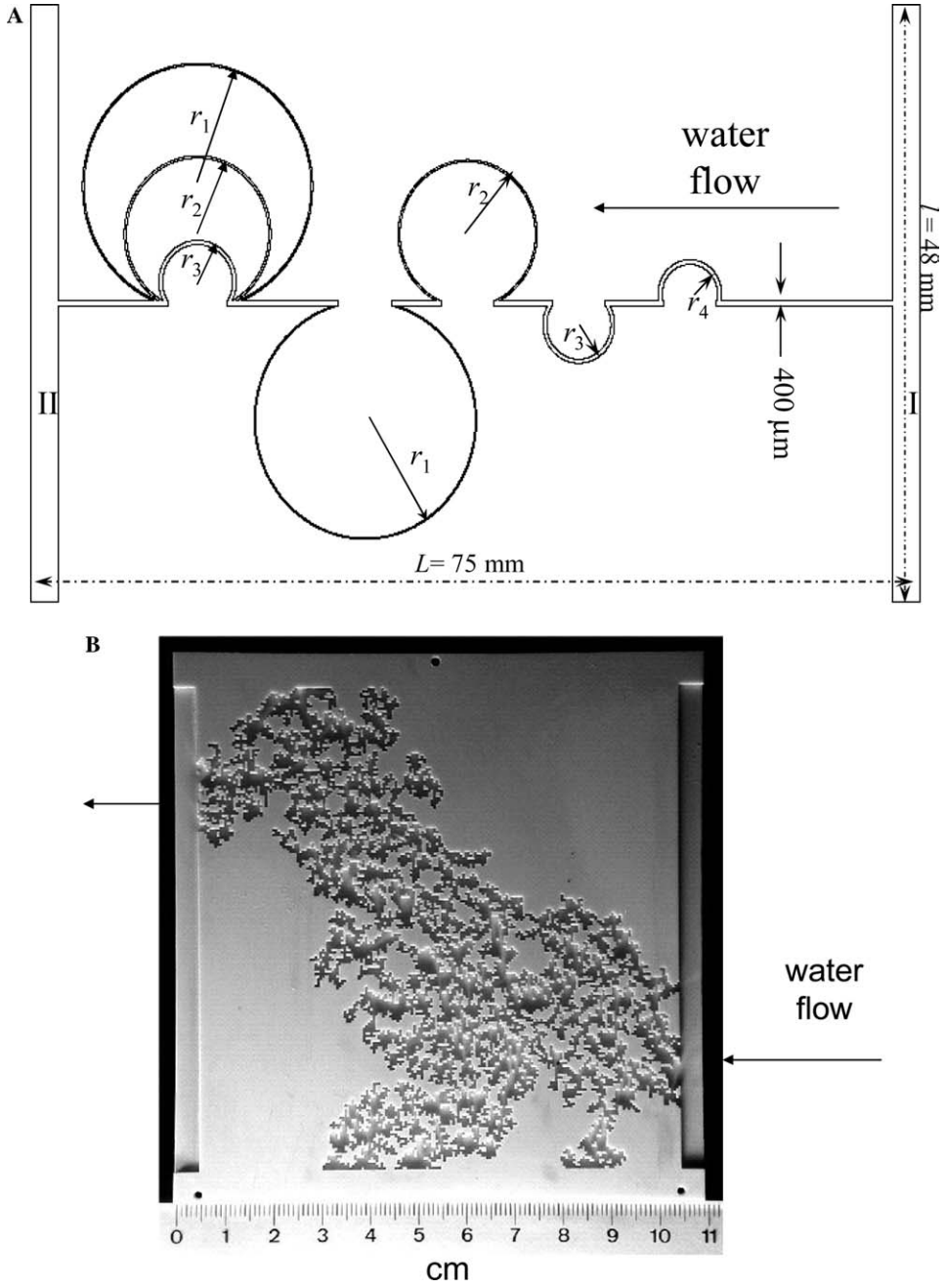

Fig. 3. Quasi two-dimensional test objects for acceleration mapping experiments and simulations. (A) Topology consisting of a series of sequential or parallel circle arc channels of various radii ($r_1 = 10.5$ mm, $r_2 = 7.5$ mm, $r_3 = 3.5$ mm, and $r_4 = 3$ mm). The depth of the channels was 2 mm and the width was 400 µm. The sections marked with ***I*** and ***II*** represent the inflow and outflow compartments, respectively. (B) Quasi two-dimensional random site percolation cluster object (photograph) based on a square base lattice of 200×200 sites occupied with a probability $p = 0.6$ which is above the percolation threshold [8,18]. The fractal dimension is $d_f = 1.9$, and the correlation length is $\xi = 1.95$ mm.

Under steady-state conditions, all explicit time dependences vanish, i.e., $\partial v_x/\partial t = \partial v_y/\partial t = 0$. The derivatives $\frac{\partial v_x}{\partial x}, \frac{\partial v_x}{\partial y}, \frac{\partial v_y}{\partial y}, \frac{\partial v_y}{\partial x}$ in relations (9) and (10) are provided by the FLUENT package. For further processing, the IDL 5.3 software was employed resulting in the desired acceleration component fields. The magnitude is then obtained from

$$a = \sqrt{a_x^2 + a_y^2}. \tag{11}$$

Note that the acceleration components given at Eqs. 9 and 10 depend on the (voxel) position but not on time since all velocity components are assumed to be locally stationary and merely change from position to position.

5. Results

Fig. 4 shows a comparison of experimental and simulated acceleration maps for the circle arc test object

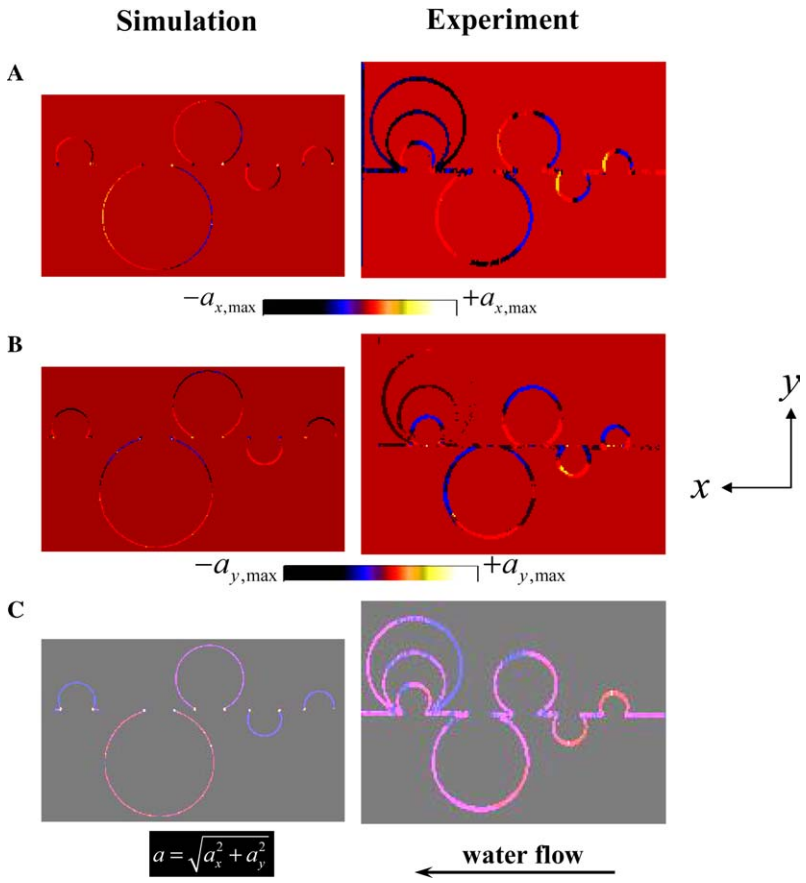

Fig. 4. Maps of the x component (A), y component (B), and the magnitude (C) of the mean acceleration for the test structure represented by Fig. 3A. The experimental data (right column) have been recorded with the aid of the pulse sequence shown in Fig. 2. The left column shows simulated data for comparison.

represented by Fig. 3A. The mean acceleration by flow in the circle arc channels is due to changes of the velocity vector direction (see components a_x and a_y in Fig. 4A and B), whereas the mean magnitude remains constant for given circle radius (see Fig. 4C).

The echo time was $T_E = 26$ ms. For a spatial resolution $\Delta x = 386$ μm the maximum velocity that can reliably be detected in the experiments is limited by $\Delta x/T_E = 14.8$ mm/s, which is within the velocity field-of-view, -90 mm/s $< v < +90$ mm/s.

The flow distribution among the three circle arc channels connected in parallel depends on the flow resistance. For a circular cross section of the channels and if Hagen/Poiseuille's law for the flow rate is valid, the flow resistance is

$$Q = \frac{\pi a^4 \Delta P}{8 L \eta}, \tag{12}$$

where L is the length of the channel section (i.e., of a circle arc with a certain radius) across which the pressure difference ΔP is exerted, η is the viscosity of the fluid, and a is the radius of the channel cross section. The channel length of the ith circle arc is

$$L_i = (2\pi - \theta_i) r_i \quad i = 1..3 \text{ and } L_1 > L_2 > L_3, \tag{13}$$

where θ_i and r_i are the angle and the radius defining the extension of the ith circle arc, respectively. The mean flow velocity is related to the flow rate according to

$$v = Q/4\pi a^2. \tag{14}$$

Combining Eqs. (12)–(14) leads to a mean flow velocity in the ith circle arc given by

$$v_i = \frac{a^2 \Delta P}{32 \eta L_i} \quad i = 1..3. \tag{15}$$

The pressure difference ΔP is the same for all three channels connected in parallel. The mean flow velocity and the channel length are consequently inversely proportional to each other, so that

$$L_1 > L_2 > L_3 \Rightarrow v_1 < v_2 < v_3. \tag{16}$$

The mean velocities v_1 and v_2 turned out to be too small to be detectable in the experiments. The same consequently applies to the acceleration. On the other hand, if the flow rate would be increased in order to make all mean velocities detectable, the problem would be that the velocity in other sections of the object would become too large.

The mean radial acceleration depends on the circle arc radius according to

$$a = \frac{v^2}{r}. \tag{17}$$

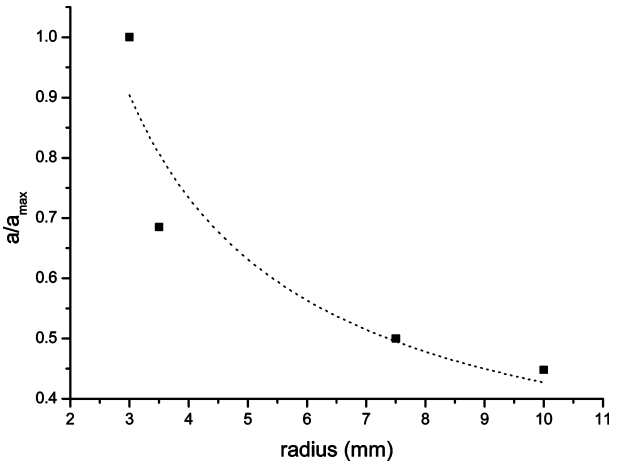

Fig. 5. Mean radial acceleration as a function of the circle arc radius in the test object represented by Fig. 3A. The black rectangles represent experimental data, and the dotted line was fitted according to Eq. (17).

Since the mean velocity in the sequential circle arcs is constant, we expect the proportionality

$$a \sim \frac{1}{r}, \tag{18}$$

which is verified in the experiments with reasonable accuracy (see Fig. 5).

Fig. 6 shows maps of the mean acceleration and mean velocity in the random site percolation cluster shown in Fig. 3B both for experimental and simulated data. All matrix voxels were blackened using a matrix mask deduced from a black-and-white converted spin density map. In this way, noise in matrix voxels whose phase would be misinterpreted by the Fourier processing analysis as a distribution of accelerations or velocities, is avoided. The flow patterns both with respect to flow velocity and acceleration are well reproduced in all cases.

The percolation cluster consist of two main components: the dead-ends that carry no flow, and the so-called backbone which is the multiply-connected part of the cluster through which the fluid flows [18,20]. The suppression of stagnant zones reveals transport pathways more clearly in the form of the cluster backbone

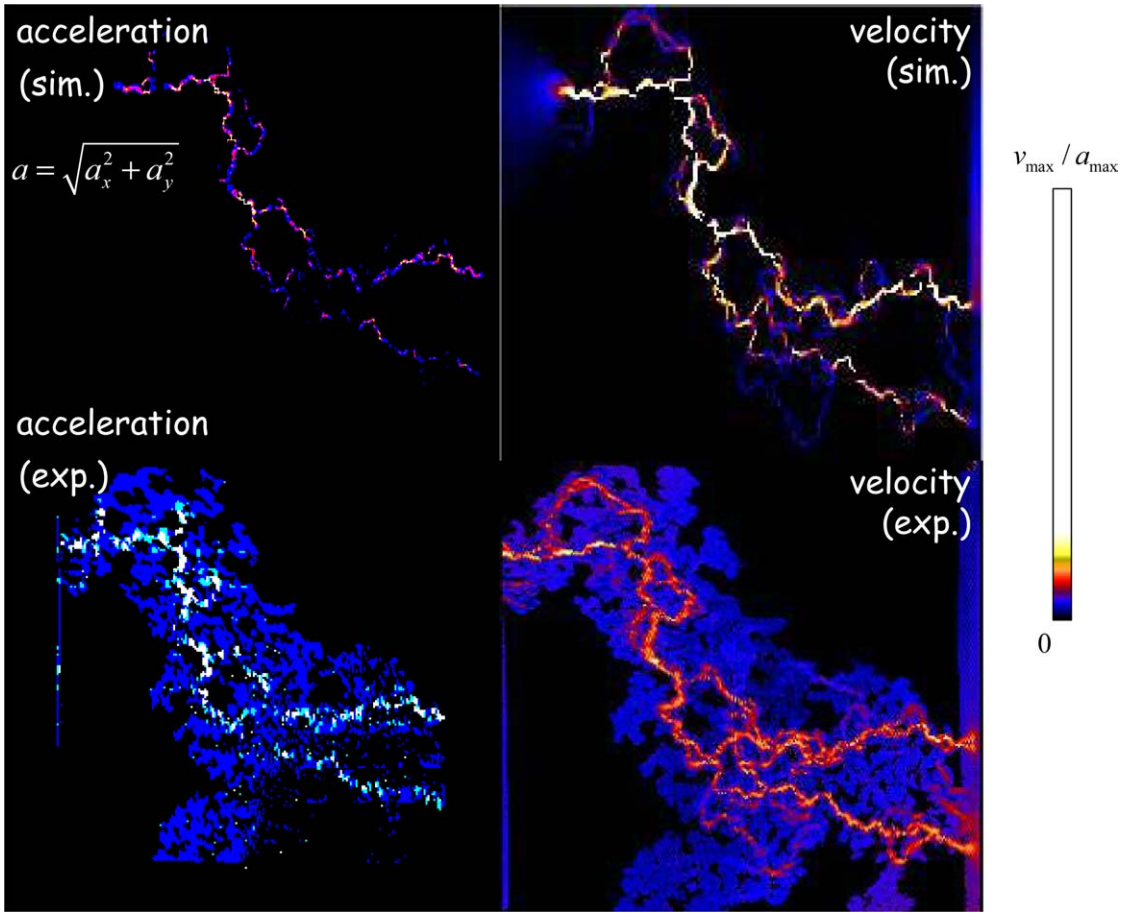

Fig. 6. Experimental and simulated maps of the mean acceleration magnitude (left column) and the mean velocity magnitude (right column) in a random site percolation cluster ($p = 0.6$, $p - p_c = 0.002$). The model object is shown in Fig. 3B.

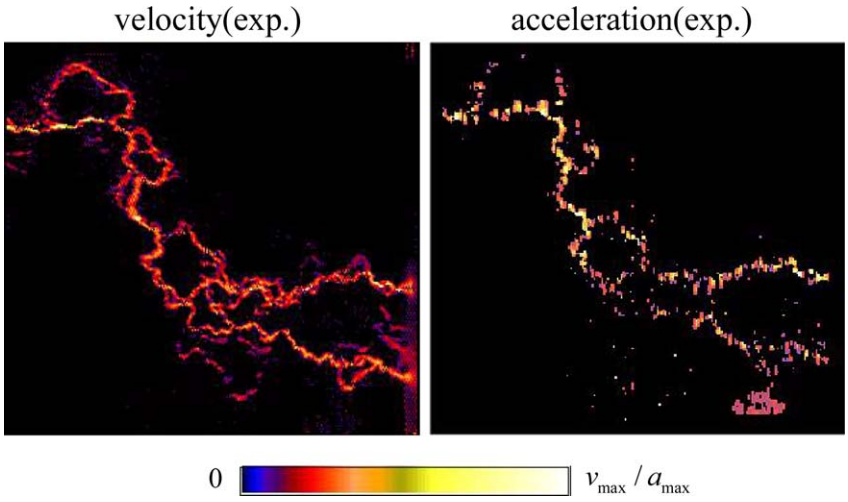

Fig. 7. "Backbones" of the experimental transport patterns shown in Fig. 6. These maps were obtained by blackening all pixels with a velocity or an acceleration below the respective noise level ($v \leqslant v_n$ or $a \leqslant a_n$). That is, all stagnant zones are removed. Only those pixels representing finite velocities or accelerations are shown.

[1]. The method used here was to black all voxels where the acceleration is below the acceleration noise level, $a \leqslant a_n$.

There are significant differences between velocity and acceleration maps (see Fig. 7). The velocity maps show pathways of a more continuous character, whereas the acceleration strongly fluctuates along the flow channels. That is, the acceleration is only in certain voxels large enough to be detectable above the noise level of the experimental set-up. These sections correspond to bottle necks and strongly curved pathways where flow is strongly accelerated or decelerated.

6. Discussion and conclusions

It was demonstrated that accelerations in flow patterns through complex porous media can directly be mapped by an NMR technique in addition to conventional flow velocity mapping. Since all transport quantities recorded by NMR microscopy techniques refer to voxel averages, the *direct* measurement of spatial acceleration distributions is considered to be more reliable than the reconstruction based on maps of the mean velocity.

Acceleration maps specifically highlight bottlenecks and strongly curved pathways of flow. They are therefore considered to be indicative for corresponding topology elements of the pore space.

In our previous papers [1–5] we pursued the strategy to use maps of transport quantities for the assessment of laws relating parameters of the pore space structure and of the transport patterns. This objective is facilitated by well-defined model percolation clusters where the pore space is defined by complete coordinate sets. Boundary conditions on this basis can be used for computational fluid dynamics simulations which then can be compared with experimental data. In all cases good coincidence was found. That is, the simulation method, the fabrication procedure of the model objects, and the NMR mapping technique are shown to be reliable and essentially free of artefacts. Simulations can thus be used to design experimental protocols and to predict the feasibility of investigations prior to the experiments. This sort of examination is expected to be useful in the broad porous media field where experimental techniques and the theoretical background are still in a rather rudimentary state [20–27].

The present study refers to (quasi) two-dimensional pore spaces. The extension to three dimensions is readily possible but time consuming, since then three four-dimensional data sets have to be acquired for the three components of the acceleration vector. In this respect a combination with fast imaging techniques is expected to be favourable [23,24].

Acknowledgments

This work was supported by the Deutsche Forschungsgemeinschaft and the Alexander von Humboldt Foundation.

Appendix A. The "polygon rule"

The gradient pulse train shown in Figs. 1 and 2 produce phase shifts proportional to stationary accelerations. Other, more complicated variants serving the same purpose exist provided that the corresponding moment conditions are fulfilled. The question to be dealt with in this appendix is whether there is a general rule

permitting one to design the simplest gradient pulse sequences for the compensation of phase shifts due to any order of motions so that phase shifts due to all higher orders become selectively relevant.

The position of a nucleus can be represented by the expansion

$$\vec{r}(t) = \vec{r}_0 + \vec{v}_0 t + \frac{\vec{a}_0 t^2}{2} + \cdots, \tag{A.1}$$

where $\vec{r}_0$, $\vec{v}_0$, and $\vec{a}_0$ are the initial position, velocity, and acceleration vectors, respectively. The phase shift in an interval T in the presence of time-varying gradients $\vec{G}(t)$ is given by

$$\phi(T) = \gamma \int_0^T \vec{G}(t) \cdot \vec{r}(t)\, \mathrm{d}t. \tag{A.2}$$

Inserting Eq. (18) gives the moment series

$$\begin{aligned}\phi(T) = \gamma \Big[& \vec{r}_0 \cdot \int_0^T \vec{G}(t)\, \mathrm{d}t + \vec{v}_0 \cdot \int_0^T \vec{G}(t) t\, \mathrm{d}t \\ & + \frac{1}{2}\vec{a}_0 \cdot \int_0^T \vec{G}(t) t^2\, \mathrm{d}t + \cdots \Big] \\ = {} & \phi_0(T) + \phi_1(T) + \phi_2(T) + \cdots. \end{aligned} \tag{A.3}$$

Motion-compensated gradient pulse trains making the diverse orders in Eq. (A.3) vanish consist of alternating gradient lobes arranged symmetrically (no 180° RF pulse in between) or inversely symmetrically (with an intermittent 180° RF pulse). The pulse trains shown in Figs. 1 and 2 are examples of the 180° pulse variant, those shown in Figs. 8 and 9 are valid in the absence of 180° pulses.

Consider now a gradient pulse train including N alternating lobes of durations $\tau_1 \ldots \tau_N$ and equal amplitudes of integer multiples of $\hat{G}$, where no RF pulses are involved. That is, rectangular gradient pulse shapes are assumed neglecting any switching ramps (see Fig. 8). The scalar vector products in Eq. (A.3) mean that only

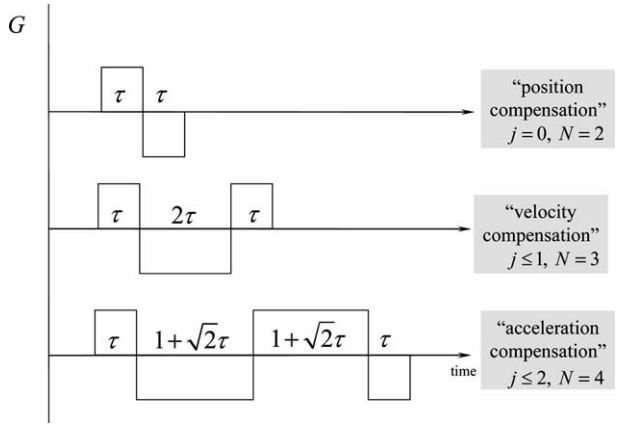

Fig. 8. Typical gradient lobe trains for the compensation of phase shifts due to positions ($j = 0$), stationary velocities ($j = 1$) and stationary accelerations ($j = 2$) in the absence of any 180° RF pulses.

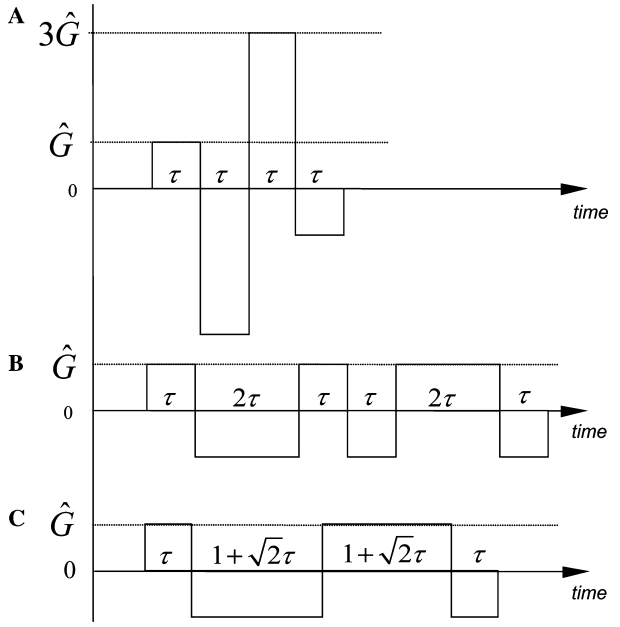

Fig. 9. Field-gradient pulse sequences for the compensation of phase shifts due to stationary accelerations: (A) Gradient pulse train based on different gradient amplitudes proposed in [25]. (B) Gradient pulse train based on alternating gradients proposed in [16]. (C) Gradient pulse train designed according to the polygon rule ($j = 2$; $N = j + 2 = 4$).

collinear components for the gradient vector and the dynamic motion vectors are relevant. We will denote these components by $\hat{G}$ and J, where J stands for r_{x0}, v_{x0}, a_{x0}, etc. The jth order phase shift thus reads

$$\begin{aligned}\phi_j(T) = {} & \frac{1}{(j+1)!}\gamma J \hat{G}\Big[2\tau_1^{j+1} + \cdots + 2(-1)^{N-1} \\ & \times (\tau_1 + \cdots + \tau_{N-1})^{j+1} + (-1)^N (\tau_1 + \cdots + \tau_N)^{j+1}\Big]. \end{aligned} \tag{A.4}$$

For example, the second-order term representing phase shifts due to stationary accelerations is

$$\begin{aligned}\phi_2(T) = {} & \frac{1}{6}\gamma a_0 \hat{G}\Big[2\tau_1^3 - 2(\tau_1 + \tau_2)^3 + \cdots + 2(-1)^{N-1} \\ & \times (\tau_1 + \cdots + \tau_{N-1})^3 + (-1)^N (\tau_1 + \cdots + \tau_N)^3\Big]. \end{aligned} \tag{A.5}$$

There is a mathematically simple method for the calculation of the gradient lobe widths leading to vanishing jth and lower order phase shifts. The number of the lobes must be $N = j + 2$. The duration of the lobes can be expressed by

$$\tau_i = \tau \frac{\sin\left(\pi \frac{i-1}{j+2}\right) + \sin\left(\pi \frac{i}{j+2}\right)}{\sin\left(\frac{\pi}{j+2}\right)}, \tag{A.6}$$

where $\tau \equiv \tau_1$. For example, if $j = 2$ and $N = 4$ we have $\tau_1 = \tau$, $\tau_2 = (1 + \sqrt{2})\tau$, $\tau_3 = (1 + \sqrt{2})\tau$, $\tau_4 = \tau$ for an acceleration compensated gradient pulse train. The

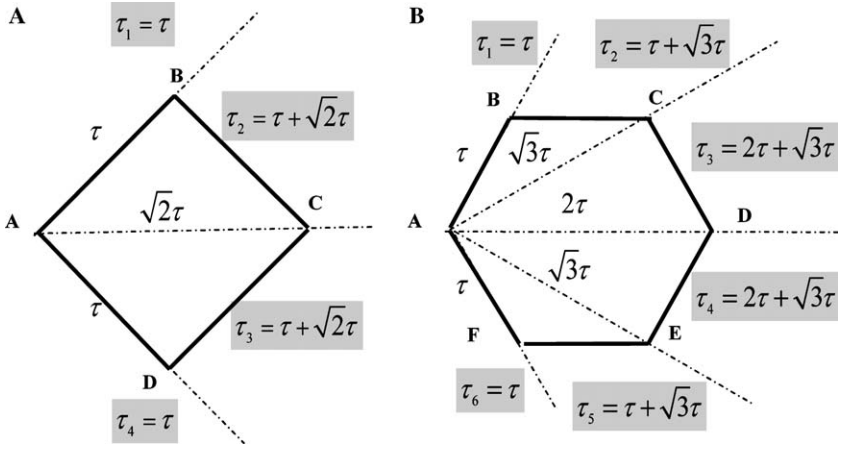

Fig. 10. The *polygon rule* for the determination of the pulse lengths implied in motion compensating gradient pulse sequences. For the compensation of phase shifts due to the jth and lower motion orders one needs $N = j + 2$ gradient lobes. The sign of the gradient lobes is alternating in the sequence of their appearance (if no phase inverting 180° RF pulse is applied in between). An N-fold polygon (solid lines) is formed with the "origin" in point A. Auxiliary rays (dotted lines) are drawn from A to the other polygon corners. The durations of the gradient lobes are then proportional to the lengths (of the first and last lobe) or double sums of adjacent line-segments (see the shadowed expressions). (A) Compensation of phase shifts due to stationary accelerations, velocities, and positions; phase encoding due to higher order motions: The maximum order to be compensates is $j = 2$. The number of gradient lobes consequently is $N = j + 2 = 4$, the polygon order 4, i.e., a square. (B) Compensation of phase shifts due to fourth and lower order motions ($j = 4$). The number of alternating gradient lobes consequently is $N = j + 2 = 6$, and the polygon order is 6.

zeroth, first and second moments vanish if the gradient pulse train takes the form (see Figs. 8 and 9C):

$$G(t) = \begin{cases} \hat{G} & \text{for } 0 \leqslant t < \tau, \\ -\hat{G} & \text{for } \tau \leqslant t < \tau(2+\sqrt{2}), \\ \hat{G} & \text{for } \tau(2+\sqrt{2}) \leqslant t < \tau(3+2\sqrt{2}), \\ -\hat{G} & \text{for } \tau(3+2\sqrt{2}) \leqslant t < \tau(4+2\sqrt{2}), \\ 0 & \text{otherwise.} \end{cases} \tag{A.7}$$

Note that this "acceleration-compensated" gradient pulse train (Fig. 9C) deviates from other sequences known from literature and represented by Figs. 8A and B [17,25–27]. The advantage of the pulse train represented by Eq. (A.7) and Fig. 9C is obvious: It is simpler than those given at Figs. 9A and B with respect to the number of lobes and the variation of the gradient strength.

There is a geometrical rule (the "polygon rule") permitting the design of motion compensating gradient pulse trains of any order. Compare Fig. 10A with Fig. 9C (or Eq. (A.7)) producing velocity compensated phase shifts proportional to accelerations. The durations of the gradient lobes are proportional to the lengths (in the case of the first and the last lobe) and double sums of adjacent line-segments forming a mesh in a rectilinear N-sided polygon, where N is the number of gradient lobes needed. Auxiliary rays originating in point A of the polygon are considered, and adjacent line sections on these rays are added to give the gradient lobe lengths.

Fig. 10B represents the polygon needed for the design of gradient pulse sequence compensating up to the sixth motion order. Six alternating lobes of duration $\tau_1 = |AB| = \tau$, $\tau_2 = |AB| + |AC| = \tau + \sqrt{3}\tau$, $\tau_3 = |AC| + |AD| = \sqrt{3}\tau + 2\tau$, $\tau_4 = |AD| + |AE| = 2\tau + \sqrt{3}\tau$, $\tau_5 = |AE| + |AF| = \sqrt{3}\tau + \tau$, and $\tau_6 = |AF| = \tau$ are suggested in this case.

References

[1] A. Klemm, H.-P. Müller, R. Kimmich, Phys. Rev. E 55 (1997) 4413.
[2] A. Klemm, R. Kimmich, M. Weber, Phys. Rev. E 63 (2001) 041514.
[3] A. Klemm, R. Metzler, R. Kimmich, Phys. Rev. E 62 (2002) 021112.
[4] M. Weber, A. Klemm, R. Kimmich, Phys. Rev. E 66 (2002) 056301.
[5] M. Weber, R. Kimmich, Phys. Rev. E 66 (2002) 026306.
[6] R. Kimmich, Chem. Phys. 284 (2002) 253–285.
[7] M.D. Mantle, A.J. Sederman, Progr. NMR Spectr. 43 (2003) 2.
[8] H.-P. Müller, J. Weis, R. Kimmich, Phys. Rev. E 52 (1995) 5195.
[9] E. Kossel, M. Weber, R. Kimmich, Solid State NMR 25 (2004) 28.
[10] C.L. Dumoulin, R.D. Darrow, D.R. Eisner, M. Tarnawski, K.T. Scott, C.G. Caro, J. Comput. Assist. Tomogr. 18 (1994) 652.
[11] P.T. Callaghan, Principles of Nuclear Magnetic Resonance Microscopy, Clarendon Press, Oxford, NY, 1991.
[12] R. Kimmich, NMR Tomography, Diffusometry, Relaxometry, Springer-Verlag, Berlin, 1997.
[13] D.O. Kuethe, Phys. Rev. A 40 (1989) 4542.
[14] D.O. Kuehte, Phys. Rev. A 44 (1991) 2495.
[15] A.J. Sederman, M.D. Mantle, C. Buckley, L.F. Gladden, J. Magn. Reson. 166 (2004) 182.
[16] B. Blümich, NMR Imaging of Materials, Clarendon Press, Oxford, 2000.
[17] Q.S. Xiang, O. Nalcioglu, IEEE Trans. Med. Imaging MI-6 (1987) 14.
[18] D. Stauffer, A. Aharony, Introduction to Percolation Theory, Taylor & Francis, London, 1992.
[19] Fluent and Gambit User's Guide Manual, Fluent Inc., July 26, 1998.

[20] M. Sahimi, Flow and transport in porous media and fractured rock, VCH, Weinheim, 1995.
[21] A. Bunde, S. Havlin (Eds.), Fractals and Disordered Systems, Springer-Verlag, Berlin, 1996.
[22] H.A. Makse, J.S. Andrade, H.E. Stanley, Phys. Rev. E 61 (2000) 583.
[23] J.L. Duerk, O.L. Simonetti, J. Magn. Reson. Imaging 1 (6) (1991) 643–650.
[24] F. Schmitt, M.K. Stehling, R. Turner, Echo-Planar Imaging, Springer, Berlin, 1998.
[25] M.S. Cohen, Motion Compensation in MR Imaging. Available from http:brainmapping.loni.ucla.edu/BMD_HTML/Shared-Code/Motion/motion.html.
[26] E.M. Haacke, Am. J. Roentgenol. 148 (1987) 1251.
[27] D. Nishimura, A. Macovski, J. Pauly, IEEE Trans. Med. Imaging MI-5 (1986) 140–151.